

Gradients of Column CO₂ across North America from the NOAA Global Greenhouse Gas Reference Network

Xin Lan^{1, 2}, Pieter Tans¹, Colm Sweeney^{1, 2}, Arlyn Andrews¹, Andrew Jacobson^{1, 2}, Molly Crotwell^{1, 2}, Edward Dlugokencky¹, Jonathan Kofler^{1, 2}, Patricia Lang¹, Kirk Thoning¹, Sonja Wolter^{1, 2}

¹National Oceanic and Atmospheric Administration, Earth System Research Laboratory, Boulder, 80303, Colorado, USA

²University of Colorado, Cooperative Institute for Research in Environmental Sciences, Boulder, 80309, Colorado, USA

Correspondence to: Xin.Lan (xin.lan@noaa.gov)

Abstract. This study analyzes seasonal and spatial patterns of column carbon dioxide (CO₂) over North America calculated from aircraft and tall tower measurements from the NOAA Global Greenhouse Gas Reference Network from 2004 to 2014. Consistent with expectations, gradients between the eight regions studied are larger below 2 km than above 5 km. The 11-year mean CO₂ dry mole fraction (XCO₂) in the column below ~330 hPa (~ 8 km above sea level) from NOAA's CO₂ data assimilation model, CarbonTracker (CT2015), demonstrates good agreement with those calculated from calibrated measurements on aircraft and towers. Total column XCO₂ was attained by combining modeled CO₂ above 330 hPa from CT2015 with the measurements. We find large spatial gradients of total column XCO₂ during June to August, with north and northeast regions having ~3 ppm stronger summer drawdown (peak to valley amplitude in seasonal cycle) than the south and southwest regions. The long-term averaged spatial gradients of total column XCO₂ across North America show a smooth pattern that mainly reflects the large-scale circulation. We have conducted a CarbonTracker experiment to investigate the impact of Eurasian long-range transport. The result suggests that the large summer time Eurasian boreal flux contributes about half of the north-south column XCO₂ gradient across North America. Our results confirm that continental-scale total column XCO₂ gradients simulated by CarbonTracker are realistic and can be used to evaluate the credibility of some spatial patterns from satellite retrievals, such as the long term average of growing-season spatial patterns from satellite retrievals reported for Europe which show larger spatial difference (~ 6 ppm) and scattered hot spots.

1 Introduction

Atmospheric measurements of carbon dioxide (CO₂) from ground and airborne platforms have greatly increased our knowledge of the global carbon cycle. Observations of CO₂, including the NOAA Global Greenhouse Gas Reference Network (GGGRN), initially emphasized ground-based measurements. These observations, started by C.D. Keeling, have monitored the CO₂ trend on both regional and global scales for over 50 years (e.g., Keeling and Rakestraw, 1960; Tans et al., 1989). In addition, the frequency and spatial distribution of airborne measurements have increased rapidly in the last two decades, providing important information about horizontal and vertical variability of atmospheric CO₂ (e.g., Gerbig et al., 2003; Choi et al., 2008; Biraud et al., 2013). Routine aircraft

36 measurements from the NOAA/ESRL GGRN monitor the large-scale distributions of a suite of trace gases,
37 including CO₂, under the influence of continental processes (Sweeney et al., 2015). A very successful approach has
38 been to employ commercial aircraft as a platform for CO₂ measurements, such as Japan's CONTRAIL
39 (Comprehensive Observation Network for TRace gases by AIRliner) project, which has provided valuable
40 information for CO₂ in the high troposphere and lower stratosphere (Machida et al., 2002; Machida et al., 2008).
41 Vertical profiles of atmospheric CO₂ reflect the combined influences of surface fluxes and atmospheric mixing.
42 Vertical profiles are particularly useful for evaluating vertical mixing in atmospheric transport models that are used
43 for inverse modeling (e.g. Stephens et al., 2007) to derive estimates of regional- to continental-scale CO₂ sources
44 and sinks (e.g., Tans et al., 1990; Gurney et al., 2002; Gurney et al., 2004; Ciais et al., 2010;).

45 While CO₂ sources and sinks are well constrained at the global scale by global mass balance, it remains
46 challenging to accurately resolve CO₂ sources and sinks at regional to continental-scale, the apportionment of which
47 depends on relatively minor variations of the observed spatial and temporal patterns of CO₂. When averaging over a
48 few months and longer the largest portion of the variations over continents results from hemispheric-scale terrestrial
49 uptake/emissions (photosynthesis)/respiration) and fossil fuel emissions, while regional net fluxes can make a
50 relatively small contribution to the signal. For example, a simple mass balance argument shows that all U.S. CO₂
51 emissions from fossil fuel burning (~1.4 Pg yr⁻¹) create a total column enhancement of only 0.6 ppm on average in
52 air parcels over the East Coast compared to the West Coast and Gulf Coast if we assume an average of 5 days for the
53 winds to flush the contiguous U.S. (~8×10¹² m²).

54 With careful calibration, air handling, and analysis, the uncertainties of in-situ measurements are less than 0.1
55 ppm. However, in-situ observation networks are sparse in global and regional coverage. Remote sensing data
56 radically increase the number of observations and capture under-sampled regions. It could have a valuable impact on
57 our understanding of the carbon cycle. However, both the precision and the potential of even very small systematic
58 biases in remote sensing measurements need to be carefully evaluated, especially those that depend on regional and
59 seasonal conditions. Vertical profiles from in-situ CO₂ measurements have been used to evaluate ground-based total
60 column XCO₂ (the "X" stands for dry mole fraction) determinations, such as those from the Total Carbon Column
61 Observing Network (TCCON) (Washenfelder et al., 2006; Wunch et al., 2010; Messerschmidt et al., 2011; Tanaka
62 et al., 2012). The uncertainty of TCCON total column CO₂ is reported to be 0.4 ppm (1σ) after comparison to
63 aircraft measurements (Wunch et al., 2010). Vertical profiles are also used to evaluate other satellite retrievals of
64 total column XCO₂, such as those from the Tropospheric Emission Spectrometer (TES)(Kulawik et al., 2013) and
65 the Greenhouse Gases Observing SATellite (GOSAT) (Inoue et al., 2013, 2016; Saitoh et al., 2016). Satellite
66 retrieval products have known and unknown biases (due to errors in spectroscopy, viewing geometry, spatial
67 differences in clouds and aerosols, surface albedo, etc.) that can result in false horizontal gradients in total column
68 XCO₂ for inverse estimates of sources (Miller et al., 2007; Crisp et al., 2012; Feng et al., 2016). After correction for
69 known biases, the mean GOSAT total column CO₂ (NIES retrievals) biases range between -2.09 to 3.37 ppm (mean
70 = 0.11 ppm, S.D.= 1.11 ppm; 20 out of 27 stations show biases lower than 1 ppm) across different aircraft sites over
71 land when compared with aircraft-based total column XCO₂ (Inoue et al., 2016). The Orbiting Carbon Observatory-
72 2 (OCO-2) retrieval of total column XCO₂ was estimated to have a mean difference less than 0.5 ppm from TCCON,

73 with RMS differences typically below 1.5 ppm after bias correction (Wunch et al., 2016). The overall uncertainty of
74 satellite retrievals is relatively large compared with the total column XCO₂ calculated from in-situ measurements.
75 Total column XCO₂ calculated from vertical profiles from the Japanese CONTRAIL project (Machida et al., 2008)
76 and from the NOAA Carbon Cycle and Greenhouse Gas aircraft program (Sweeney et al., 2015) complemented with
77 simulated profiles from a chemistry–transport model above the maximum altitude of the data have uncertainty less
78 than 1 ppm (Miyamoto et al., 2013). The smaller uncertainty of the in situ-based total column XCO₂ suggests that
79 they can be used to evaluate satellite retrievals of column averaged CO₂. Since aircraft profiles co-located with
80 satellite retrievals are rare, it is useful to consider the statistics of total column XCO₂ fields derived from repeated
81 aircraft profiles over particular locations.

82 The effect of satellite column averaging kernels and a priori profiles when comparing aircraft-based column
83 XCO₂ with GOSAT retrievals has been assessed by Inoue et al. (2013). For the case considered, application of the
84 averaging kernel and a priori profile to simulate total column XCO₂ was generally within ± 0.1 ppm of the density
85 weighted total column, suggesting that the averaging kernels can only account for small part of the overall
86 uncertainty of the GOSAT total column XCO₂ (Inoue et al., 2013).

87 Transparent and objective estimates of CO₂ sources and sinks derived from atmospheric measurements are
88 essential for validating emissions reduction efforts and other mitigation policies, and for lowering the uncertainties
89 of carbon cycle-climate feedbacks. The latter are major ambiguities in predicting future climate, such as potential
90 uncontrolled CH₄ and CO₂ emissions from warming permafrost in Arctic regions. Satellite retrievals of total column
91 XCO₂ can significantly improve estimates of sources and sinks only if they are sufficiently precise and accurate (
92 Houweling et al., 2004; Chevallier et al., 2014), meaning that even very small systematic errors (biases) must be
93 eliminated. Here, we analyze the spatial and temporal variability of column CO₂ over North America using well-
94 calibrated CO₂ measurements from aircraft and tall tower, and we use model results from NOAA’s CarbonTracker,
95 version CT2015 (Peters et al. 2007, with updates documented at <http://carbontracker.noaa.gov>) to investigate the
96 primary drivers of variability in total column XCO₂. The aircraft data enable direct analysis of column CO₂
97 characteristics, which is the fundamental step for accurate apportionment of sources and sinks. This study focuses on
98 long-term averaged column CO₂ gradients and the contributions of different vertical layers to the total column
99 variability. It can serve as a reference for evaluating regional and seasonal biases of current and future column CO₂
100 retrievals from both ground and satellite platforms.

101 **2 Methods**

102 **2.1 Aircraft and tall tower sampling**

103 Aircraft sampling in the NOAA GGGRN intends to provide vertical profiles of long-lived trace gases to capture
104 their seasonal and interannual variability. The aircraft sampling system consists of 12 borosilicate glass flasks in
105 each programmable flask package (PFP), a stainless-steel gas manifold system, and a data logging and control.
106 These flasks (0.7 L each) are pressurized to obtain 2.2 L of sample air from each target altitude. Air samples are then
107 shipped back to NOAA/ESRL for carefully calibrated and quality-controlled measurements. Carbon dioxide is

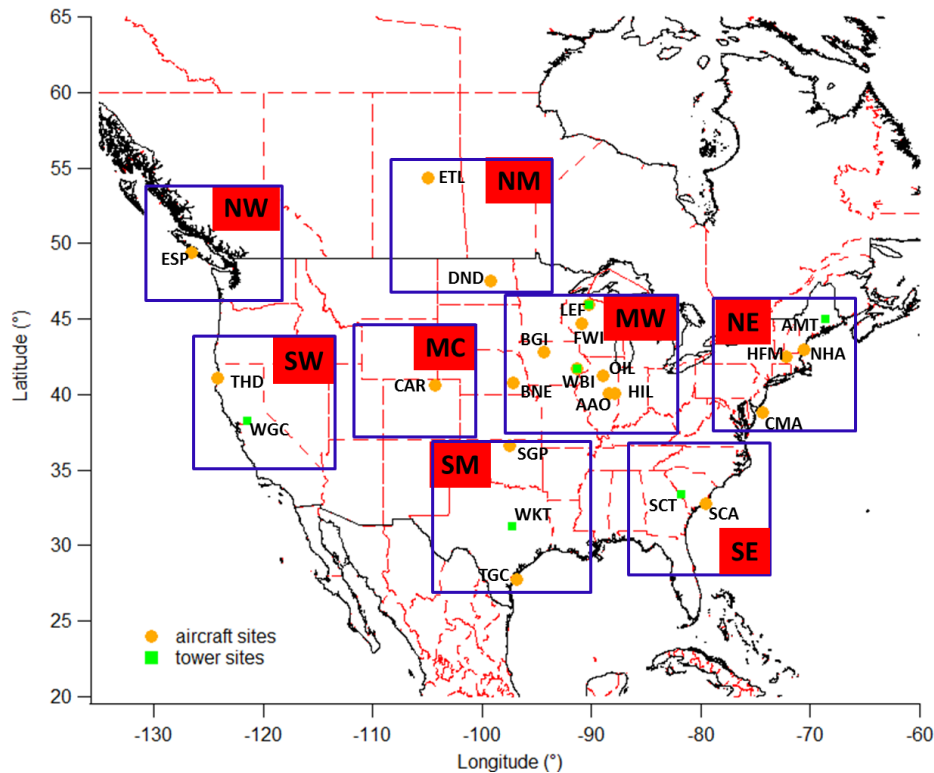
108 measured using a nondispersive infrared analyzer. Long-term measurements at ~15 sites are carried out using light
109 aircraft that can reach 8.5 km. Air samples are collected mostly during late morning to early afternoon, when the air
110 mass within the planetary boundary layer (PBL) is generally well mixed, and CO₂ enhancement near the ground
111 from plant respiration during the night has been mixed throughout the boundary layer. Normally, the aircraft follows
112 a pre-decided route such that most samples are collected within 0.1° of the site location. The sampling frequency
113 varies from site to site, currently from twice a month to once every 1.5 months. For more sampling details, quality
114 control discussions, and an evaluation of the sampling frequency, please refer to Sweeney et al. (2015). More
115 information on the aircraft sites can be found at <http://www.esrl.noaa.gov/gmd/ccgg/aircraft/>. We estimate the
116 uncertainty of individual measurements of CO₂ in flask air (68% confidence level) at 0.08 ppm. However, we have
117 seen evidence of positive biases for samples collected using older flasks that may contain contaminants. Andrews
118 et al. (2014) reported biases that increased from <0.1 ppm in 2008 to an average offset in 2013 of 0.36 ppm. The
119 aircraft sampling protocol was modified starting in August 2014 to mitigate this bias. For samples collected prior the
120 protocol change, laboratory tests showed that new/clean flasks have zero bias, but some older/dirty flasks could have
121 biases of > 1 ppm. This bias is not consistent among individual flasks and increasing over time (Andrews et al.,
122 2014), the potential bias is hard to quantify for measurements before August 2014. Thus, the high bias is not
123 corrected in our study. More recently, low bias has been found in PFP measurements when the ambient humidity is
124 high, based on comparisons of PFP measurements with data from in-situ analyzers at tall towers. We are working to
125 understand and quantify this bias, and for this study we have derived a preliminary correction factor, which shows a
126 linear trend with -1.4 ppm CO₂ offset per 1% above 1.7% of ambient water (mole fraction relative to whole air)
127 content. Only ~ 4% of total aircraft measurements or ~ 12% of those below 2 km are impacted by humidity higher
128 than 1.7%, for which we have applied corrections before data analysis. The mean correction applied is 0.53 ± 0.4 (1
129 σ) ppm for the impacted data.

130 The NOAA tall tower network measures CO₂ and other trace gases within the continental boundary layer.
131 Continuous in-situ measurements are conducted using nondispersive infrared (NDIR) absorption sensors and cavity
132 ring-down analyzers. The long-term stability of these systems is typically better than 0.1 ppm for CO₂ (Andrews et
133 al., 2014). Most tall tower sites have more than one air intake height. In this study, continuous in-situ measurements
134 from the highest intake are used to minimize potential influences from local sources. More information concerning
135 the tower sites can be found at <http://www.esrl.noaa.gov/gmd/ccgg/insitu/>. For the column XCO₂ calculation, tower
136 data only from 10:00-17:00 local standard time (LST) on flight days are averaged to one data point per day, as a
137 complement to vertical profiles within the PBL.

138 **2.2 Site description**

139 We analyze data from 19 aircraft sites and 6 tall tower sites during 2004 to 2014 (see Table S1 for a summary of site
140 conditions). After considering the geographic distribution of these sites in North America, we group them into eight
141 regions for spatial comparisons (Fig. 1). The northern west (NW) and southern west (SW) regions represent the
142 inflow area in the west coast of US, directly downwind of the Pacific Ocean at both higher elevations. The northern
143 mid-continent (NM) region represents the boreal forest and agriculture region in north-central North America. The

144 mid-continent (MC) region represents a dry landscape due to its high elevation (above 1.5 km on average) and semi-
 145 arid climate. The mid-west (MW) region is strongly influenced by agriculture and temperate forest. The southern
 146 mid-continent (SM) represents the south-central humid temperate region, with inflow from the Gulf of Mexico
 147 during summer. The northeast (NE) region represents the temperate forest in north-east coast of U.S., which is
 148 mostly downwind of regions to the west above the PBL, and downwind of its south-west regions within the PBL.
 149 The southeast (SE) region represents the warm temperate region in the south-east coast of U.S.
 150

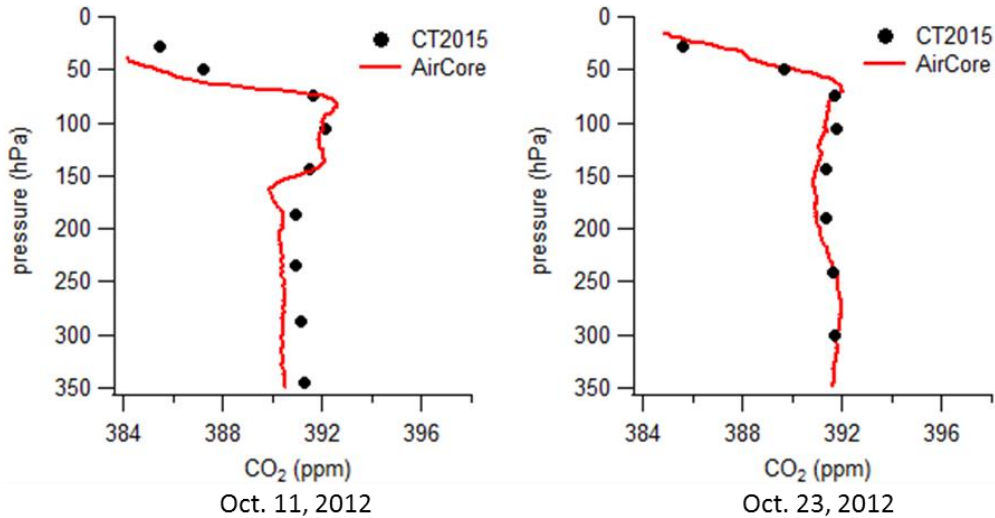


151
 152 **Fig. 1.** Aircraft, tall tower, and high elevation/tower sites in the NOAA GGGRN. The eight boxes define regions
 153 that are further discussed for spatial pattern comparison.

154 **2.3 Smoothing of the reference data and column XCO₂ calculation**

155 We use Mauna Loa Observatory (MLO) as a reference site. MLO is located at 19.536°N, 155.576°W, and 3397 m
 156 above sea level. Carbon dioxide measurements from this site are widely used to represent background CO₂ in the
 157 Northern Hemisphere. For our study, a function consisting of a quadratic polynomial and four harmonics is fitted to
 158 the MLO data, adopted from the method described by Thoning et al. (1989). Residuals of the data from this function
 159 are smoothed by a low-pass filter with full-width at half-maximum in the time domain of 1.1 years. The smoothed
 160 residuals are then added back to the polynomial part of the function to produce the long-term deseasonalized trend.
 161 This trend (see Fig. 3) is subtracted from all aircraft and tall tower measurements. Also, the CarbonTracker results
 162 presented in this study are the differences relative to observed MLO deseasonalized trend. We use ‘Δ’ to represent
 163 detrended data in the following text and figures. The choice of reference site is not important for this study, since

164 we focus on examining the relative seasonal patterns of the detrended spatial and vertical distributions of CO₂
165 instead of the total changes in CO₂ abundance attributed to global surface fluxes.
166



167
168 **Fig. 2.** Carbon Tracker (CT2015) simulations compared with AirCore in-situ measurements in upper atmosphere.
169 AirCore profiles in the left and right panels are sampled near CAR and SGP, respectively.

170
171 We calculate partial column average CO₂ dry mole fraction using tall tower and aircraft data, and the total
172 column by adding simulations of high altitude CO₂ (above 330 hPa, ~ 8 km above sea level) from CarbonTracker.
173 Since geometric height from the onboard Global Positioning System (GPS) (after 2006) or inferred from the aircraft
174 altimeter or pressure altitude is archived with each aircraft measurement, we first convert geometric height (in
175 meter) to pressure (in hPa) for the pressure-weighted column XCO₂ calculation. This conversion uses geopotential
176 data from NOAA/NCEP North American Regional Reanalysis (NARR) (Mesinger et. al, 2004), available at
177 <https://www.esrl.noaa.gov/psd/data/gridded/data.narr.html>, in which the geopotential is a function of latitude,
178 longitude, pressure altitude and time. We interpolate the geopotential field vertically to retrieve pressure, and then
179 calculate dry pressure by incorporating specific humidity data from NARR. Eventually we use a trapezoidal method
180 to integrate over detrended vertical profiles for dry-pressure-weighted column averages. For the long-term averaged
181 column ΔXCO₂ calculation, a long-term mean vertical profile is first constructed for each month by combining 11-
182 year detrended data together and then average data in each 40 hPa vertical bin. To look at the long-term averaged
183 total column ΔXCO₂ from individual aircraft sites, we combine aircraft data with upper-layer CT2015 simulations.

184 The NOAA CarbonTracker model assimilates CO₂ measurements from surface sampling networks and tall
185 towers to generate global 3D fields of atmospheric CO₂ mole fraction. The Carbon Tracker model has evolved
186 significantly since Peters et al. (2007). A detailed description of this model is provided in documents available at
187 <http://carbontracker.noaa.gov>. Our study utilizes CarbonTracker results from the 2015 release (CT2015), publicly
188 accessible at <ftp://aftp.cmdl.noaa.gov/products/carbontracker/co2/CT2015/molefractions/>. This version provides
189 CO₂ mole fraction over North America with 1° × 1° spatial and 3 hour temporal resolutions, which are analyzed in

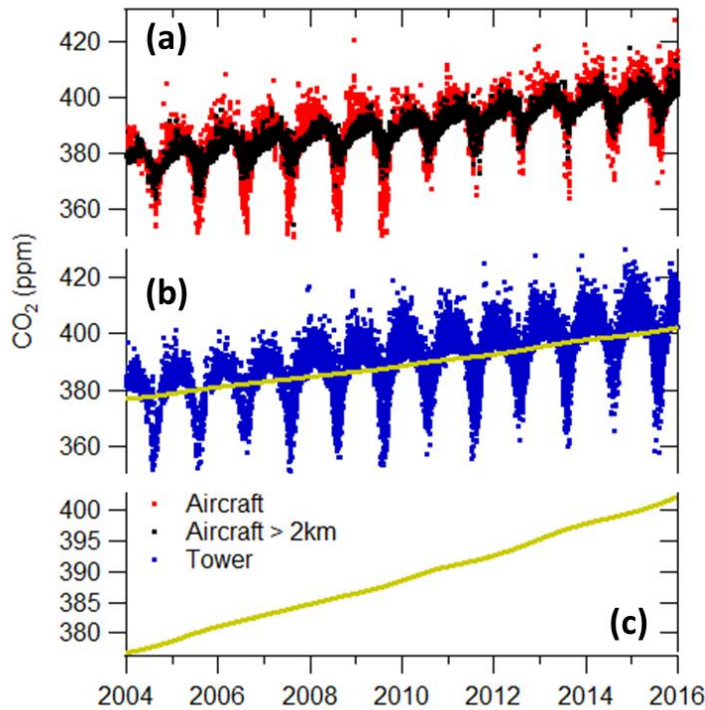
190 Sect. 3.2 and 3.3. Total column CO₂ calculated from CT2015 global data with 3° × 2° spatial resolution is also
191 presented in the supporting information (SI). We have evaluated the performance of CarbonTracker in upper
192 atmosphere (330 to 0 hPa) by comparing its simulations with in-situ measurements from 9 AirCore profiles (Karion
193 et al., 2010) sampled in 2012-2014. AirCore is a ~150 m stainless steel tube that utilizes changes in ambient
194 pressure for passive sampling of the vertical profile. The tube is carried to high altitude by balloon and it collects a
195 continuous sample as it descends. It is then measured by an analyzer after it is recovered. More information about
196 AirCore system can also be found at <https://www.esrl.noaa.gov/gmd/ccgg/aircore/>. All 9 AirCore profiles are taken
197 near SGP and CAR sites. Figure 2 shows examples of AirCore profiles compared with CT2015 in the upper
198 atmosphere, which demonstrates good agreement. We also compare partial column (330 to 0 hPa) averages from the
199 9 AirCore profiles and CT2015. Results from CT2015 agree generally well with AirCore, with difference ranging
200 from 0.03 to 1.22 ppm (mean value equals 0.66 ppm), which suggests that CT2015 may have a high bias that could
201 contribute to $0.66 \times 1/3 = 0.22$ ppm overestimate on average to the total column average. However, AirCore is in the
202 process of rigorous evaluation, the differences between AirCore and CT2015 are not well characterized yet since we
203 only have a limited amount of AirCore data. It is unclear whether the potential bias of CT2015 in this partial column
204 is dependent on time or sampling location. Adding a constant bias correction to all regions will not change the
205 spatial gradients that we focus on in this study. Thus no correction is applied when using CT2015 simulations to
206 represent the upper 1/3 of the total column. For uncertainty estimates, we use a “bootstrap”
207 method that uses random resampling of individual vertical profiles with restitution (low bias, high humidity was
208 corrected), with 100 Monte Carlo runs for each column average calculation. Uncertainty is then defined as one
209 standard deviation of the 100 Monte Carlo results.

210 **3 Results and Discussions**

211 **3.1 Seasonal patterns and spatial gradients**

212 Typically one aircraft profile contains measurements at 12 different altitudes. Column ΔXCO_2 can be computed for
213 each profile using the method described in Sect. 2.3 (Fig. S1). Our aircraft and CT2015 based column CO₂ at SGP
214 and LEF sites shows reasonable agreements with TCCON data retrieved at Lamont and Park Falls site
215 (Washenfelder et al., 2006; Wunch et al, 2009, 2011), respectively (Fig. S2). Figure 3 shows aircraft (at all altitudes)
216 and tower data (daily averages for 10:00-17:00 LST data) from all sites used in this study. Aircraft data above 2 km
217 exhibit much smaller seasonal variations than the full dataset, because the variations are mainly driven by CO₂
218 sources and sinks near Earth’s surface. CO₂ mole fraction is enhanced in the shallow wintertime PBL primarily due
219 to reduced plant photosynthesis and ecosystem respiration combined with slightly increased fossil fuel emissions.
220 During summer the PBL is deeper, and depletions within the PBL are due to strong terrestrial uptake that dominates
221 over emissions especially during June through August. During summer of 2010 to 2012, CO₂ from aircraft
222 measurements appears higher than other years in Fig.3; however, similar characteristics are not present in tower
223 data. This apparent difference is due to a decrease in sampling frequency at several aircraft sites that resulted in an

224 aliased picture of the full summer signals. Since we focus on climatological mean of 11 years of data in our study,
225 this influence is eliminated by combining 11 years of data together into one “average year”.



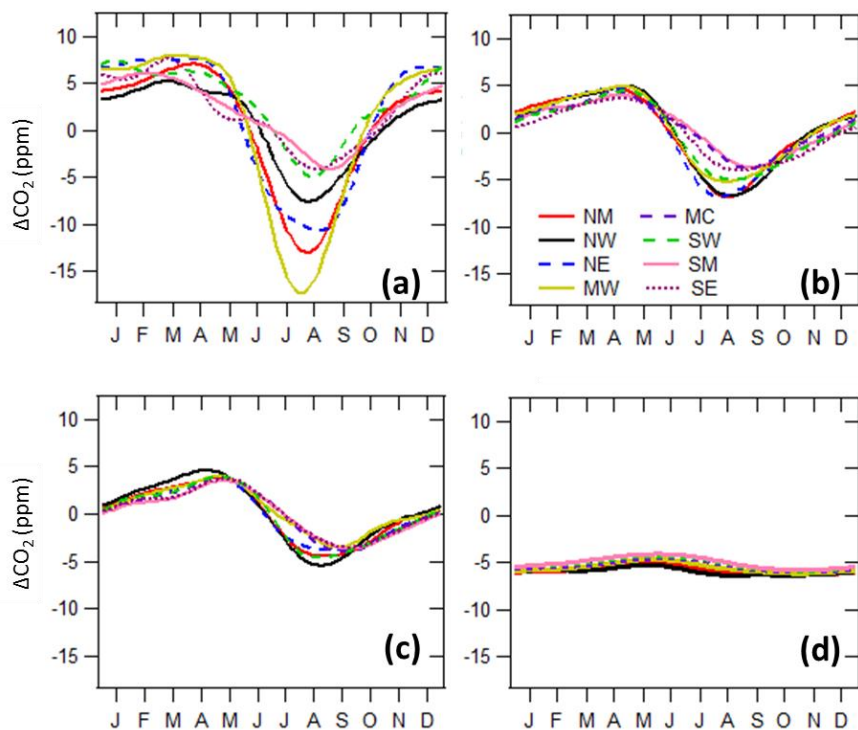
226
227 **Fig. 3.** CO₂ observations from aircraft (a) and towers (b). The yellow line in (b) illustrates the deseasonalized trend
228 at Mauna Loa (MLO), same as in (c), in which y-axis is expanded.

229
230 To investigate the contributions of different altitudes to spatial gradients between regions, we divided all
231 measurement data into three layers according to their sampling altitudes: below 2 km, 2 - 5km, and 5 - 8.5 km masl
232 (Fig. 4). Smooth seasonal curves are attained from fitting data with four harmonics using the method described by
233 Thoning et al. (1989). The peak-to-valley amplitudes of the seasonal cycles below 2 km are the largest among the
234 three layers for most regions, with a minimum of 10.3 ppm in SM and a maximum of 25.0 ppm in MW. The
235 seasonal variation amplitudes decrease to 7.7-11.5 ppm in the 2 - 5 km layer, and further decrease to 7.2-10.0 ppm in
236 the 5 - 8.5 km layer. We also observe that the seasonal cycle drawdown occurs later in the layers above 2 km (see
237 Fig. S3, which provides similar information as Fig. 4, but seasonal curves from different vertical layers are grouped
238 by regions to facilitate comparisons of the phases of seasonal cycles). The seasonal CO₂ drawdown below 2 km is
239 mainly influenced by terrestrial photosynthesis and gradients are due to local to regional fluxes, with an earlier onset
240 of drawdown in southern regions than in northern regions. The seasonal cycle aloft is damped and lagged compared
241 to the PBL, with influences from throughout the Northern Hemisphere and with spatial gradients likely driven by
242 large-scale transport. The NW, SW, SM, and SE inflow regions have significant delays of more than one month in
243 the 2 - 5 km layer compared with the surface layer, which is likely due to the delayed phase of the seasonal cycle in

244 well-mixed air coming from the oceans. Vertical homogeneity of air over ocean was observed during the HIAPER
245 Pole-to-Pole Observations (HIPPO) aircraft campaign (Wofsy et al., 2011; Frankenberg et al., 2016). As air masses
246 are transported further inland, we observe reduced discrepancies of the timing of CO₂ drawdown between surface
247 and upper layer air (2-5 km), which may be associated with the increased influence of the land surface in the mid-
248 troposphere due to strong convection over land. CO₂ drawdown in the 5 - 8.5 km layers also occurs later than in the
249 2 - 5 km layers in most regions; however, differences between these two layers are small. The declining amplitude
250 and delayed phase of the seasonal cycle with altitude have been noted often (e.g., Tanaka et al., 1983; Ramonet et
251 al., 2002; Gerbig et al., 2003, Sweeney et al. 2015). It demonstrates that there is lot of important information in the
252 vertical profile that is diminished in observations of the total column.

253 We find that the largest horizontal spatial gradients between regions occur below 2 km during summer time
254 (Fig. 4), with a maximum difference of ~15.5 ppm between MW and SM. SM and SW exhibit less pronounced
255 seasonal cycles, which is likely associated with air masses from the Gulf of Mexico and the Pacific Ocean,
256 respectively, whereas MW exhibits a deep summer drawdown (amplitude in seasonal cycles) partially as a result of
257 strong regional forest and crop uptake. Crevoisier et al. (2010) estimated the surface flux over North America using
258 vertical CO₂ measurements and average wind vectors, and reported that annually averaged land carbon fluxes in the
259 western (including SW region) and southern regions (including SM region) were neutral. The SE region also
260 demonstrates a less pronounced seasonal cycle with higher summertime levels compared with other northern
261 regions, which may be due to the sea-breeze influence in summer within PBL. In wintertime, CO₂ levels in NE and
262 MW are higher than in other regions, which result from regional fossil fuel and terrestrial biogenic emissions
263 combined with transport from the west and south.

264 Higher altitude data (above 2 km) exhibit only small spatial gradients. In the 2 - 5 km layer, the largest gradient
265 is 4 ppm in summer (Fig. 4b). It further decreases to less than 3 ppm in the 5 - 8.5 km layer (Fig. 4c). Figure 4d
266 shows modeled CO₂ mole fractions from CT2015 for the upper troposphere and above (330 hPa to 0 hPa), which are
267 used to fill in above the aircraft profiles for calculation of total column ΔX_{CO_2} . Spatial gradients in this layer are
268 less than 0.5 ppm, suggesting that the top third of the total column has little contribution to the spatial gradients of
269 the total column.



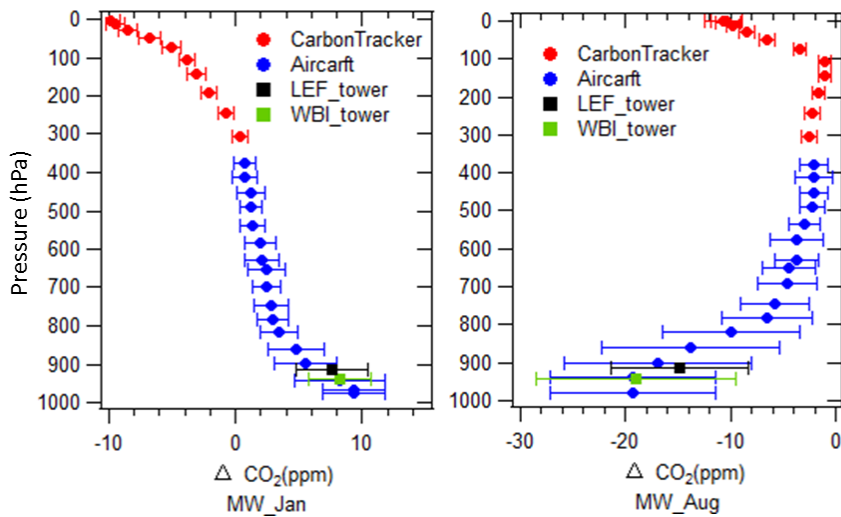
270
 271 **Fig. 4.** Multi-year (2004-2014) average smooth seasonal curves of CO₂ relative to the long-term de-seasonalized
 272 trend at Mauna Loa for different vertical layers: (a). Aircraft and tower data under 2 km, MC is not presented
 273 because only limited data were available due to high surface elevations (>1.5 km on average) in this region; (b).
 274 Aircraft data from 2 - 5 km; (c). Aircraft data from 5 - 8.5 km; (d). CT2015 model results for layers above 330 hPa
 275 (~8.5 km) to 0 hPa (~80 km).

276 3.2 Long-term mean vertical profiles

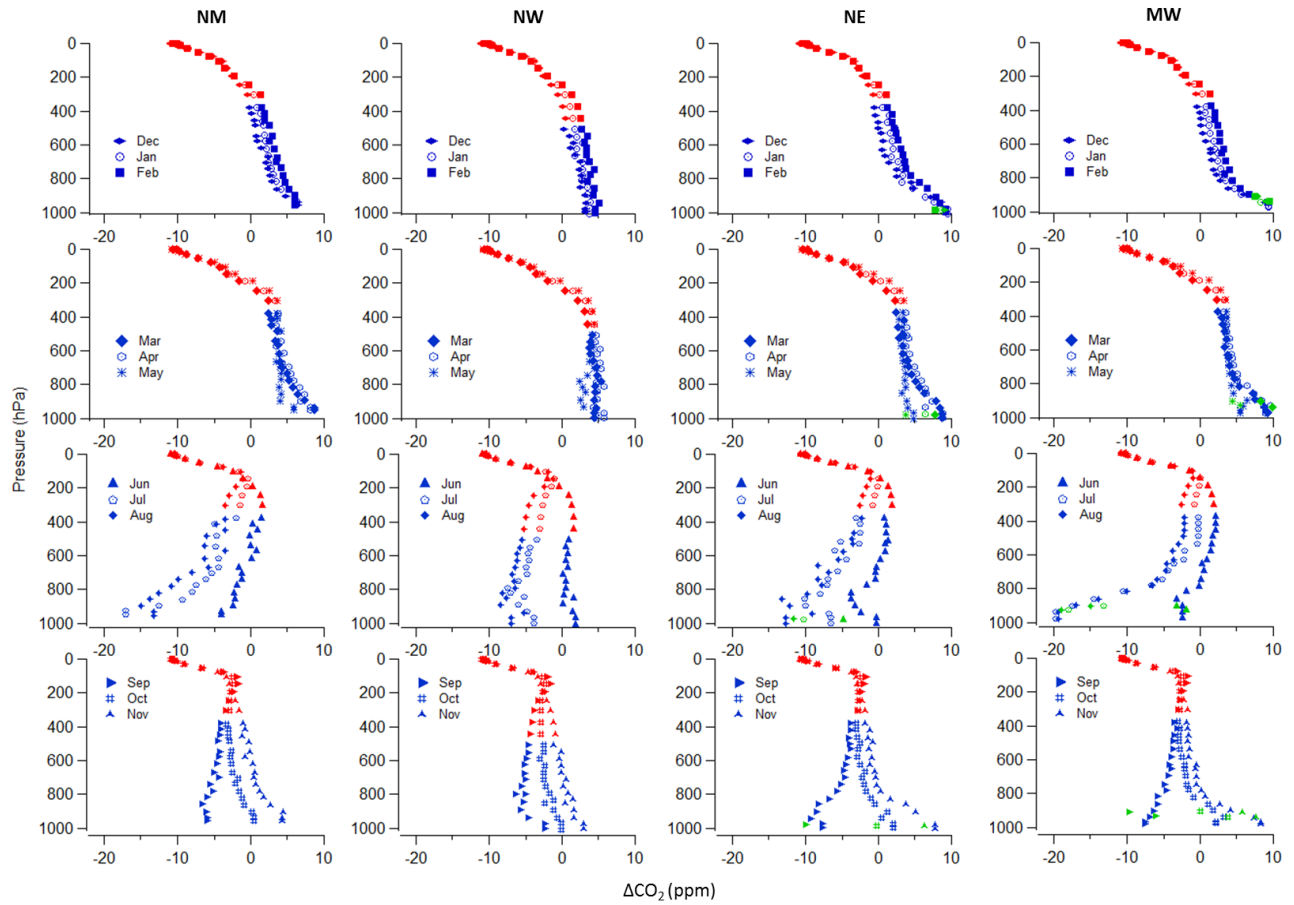
277 To investigate the mean spatial gradients, we first calculate the long-term mean monthly vertical profiles as
 278 described in Sect. 2.3. In addition, each tower serves as one additional layer in the mean profile. The long-term
 279 mean tower data generally fit well in the vertical profiles from measurements of aircraft samples (Fig. 5 and Fig. 6),
 280 suggesting that the biases described in Sect. 2.1 above do not significantly affect the long-term mean. To attain
 281 profiles of the entire atmospheric column, upper layers (330 to 0 hPa) are filled in by CT2015, and the lowest data
 282 point of the measured profile is extended to ground level, defined by the mean surface elevation in that region.

283 Figure 5 presents two examples of long term mean profiles with data variability, which is the one standard
 284 deviation for each 40 hPa bin of aircraft data or for all flight-day tower data. Variability as large as 20 ppm is seen
 285 within the PBL in the MW region in summer, which is due to strong and heterogeneous surface vegetation uptake
 286 and ecosystem respiration combined with day-to-day changes in wind direction. All long-term mean monthly
 287 vertical profiles are presented in Fig. 6, which shows the mean temporal and vertical variability of CO₂ in each
 288 season, and further demonstrates the vertical propagation of seasonal CO₂ due to changes of surface flux. In

289 wintertime, monotonic decrease of CO₂ with altitude can be observed from all regions, in which high PBL CO₂ is
 290 mainly driven by surface emissions and reduced vertical mixing (Denning et al., 1998; Stephens et al., 2007).
 291 Surface CO₂ decreases dramatically in the growing season in those regions influenced by high plant activity, such as
 292 NM and MW regions. For the summer vertical profiles in NE and SE region (east coast of the U.S.), the CO₂ mixing
 293 ratio is elevated in the layer under 900 hPa followed by significant decreases in upper layers until 750 hPa, and then
 294 increases with altitude until tropopause (Fig. 6). This is likely a result of sea breeze influence. Lower-troposphere air
 295 from the sea, lacking terrestrial uptake of CO₂, typically has higher CO₂ in summer compared with inland air.
 296 Polluted air previously advected offshore can be brought back along with sea breeze. Without significant vertical
 297 mixing over the marine surface, high levels of pollutants remain in those air masses. The convergence of sea breeze
 298 with prevailing wind moving offshore may create a period with a stalled frontal structure that can aggregate air
 299 pollutants (Banta et al., 2005). The convective internal boundary layer structure of the sea breeze system can
 300 significantly reduce mixing height (Miller et al., 2003), and also induces higher CO₂ levels. When the sea breeze is
 301 not dominant, air advected from southwest and west (the land) can also bring in polluted air with high CO₂ since this
 302 region is downwind of continental U.S. emissions (Miller et al., 2012).

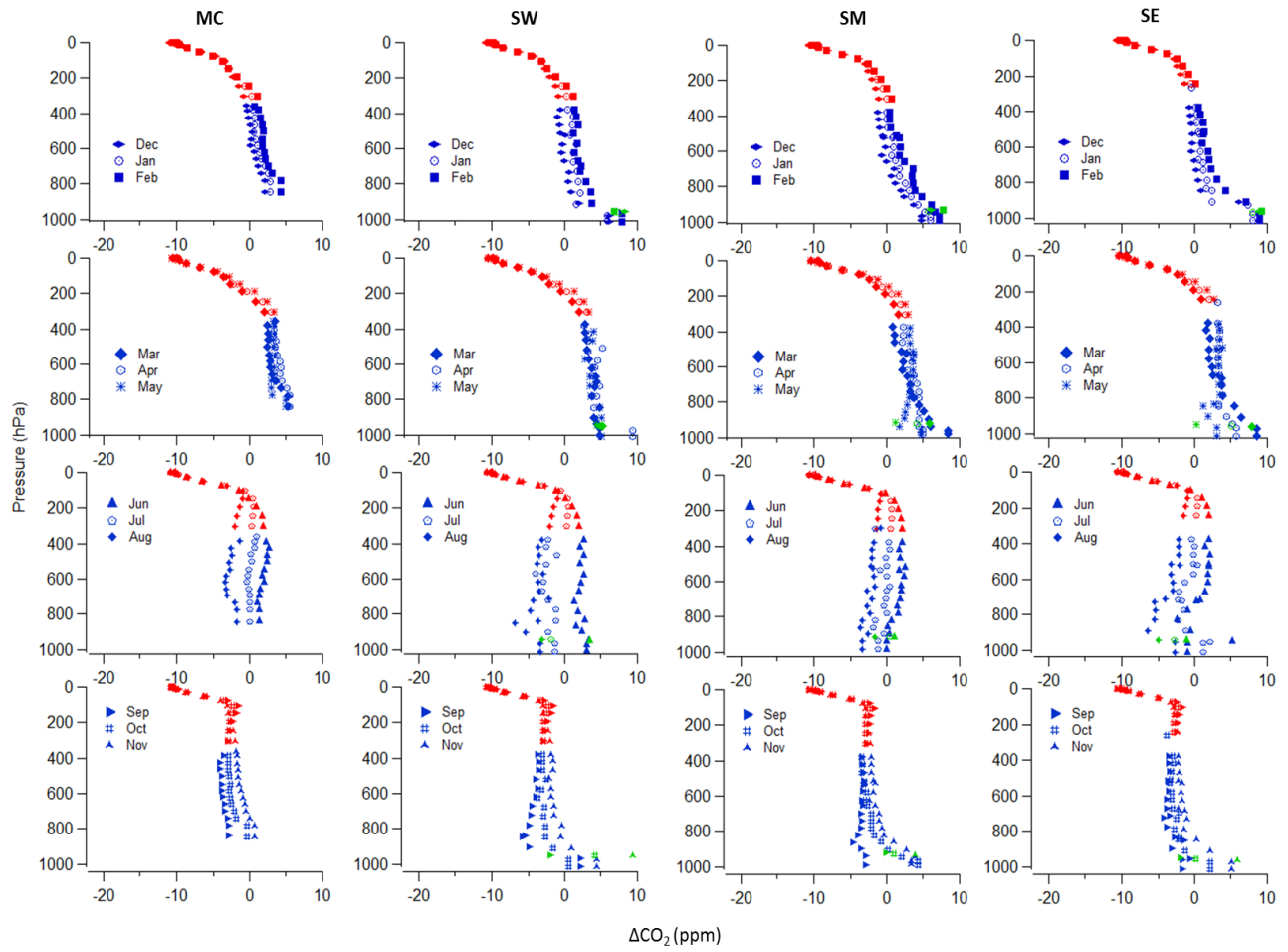


303
 304 **Fig. 5.** Long-term mean (2004-2014) average vertical profiles in January (left panel) and August (right panel) in
 305 region MW. Error bar shows one standard deviation.



306

307 **Fig. 6a.** Long-term mean (2004-2014) monthly vertical profiles in NM, NW, NE, MW (by column, from left to
 308 right). Blue points were calculated from observations, red points were calculated from CT2015, and green points
 309 were calculated from tower data.



310

311 **Fig. 6b.** Long-term mean (2004-2014) monthly vertical profiles in MC, SW, SM, SE (by column, from left to right).

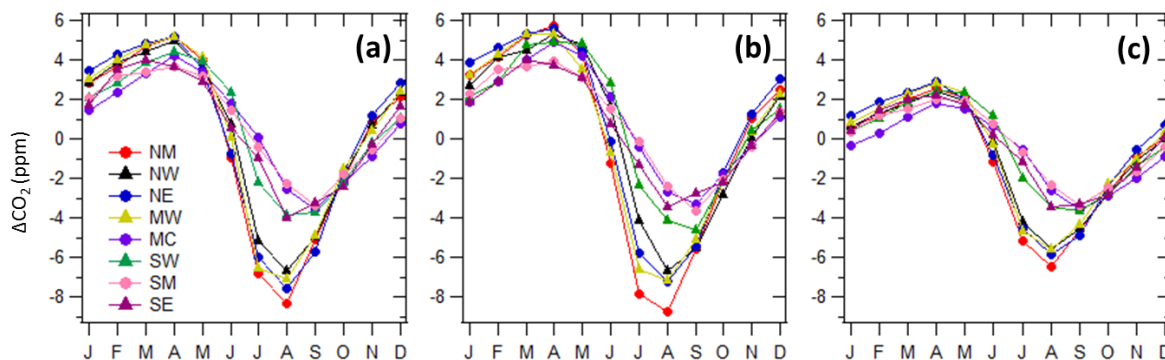
312 Blue points were calculated from observations, red points were calculated from CT2015, and green points were

313 calculated from tower data.

314

315 3.3 Partial column ΔXCO_2 and total column ΔXCO_2

316 Seasonal variations of monthly averaged partial column ΔXCO_2 (below 330 hPa) demonstrate maximum values in
317 April and minimum values in August or September (Fig. 7a). The largest amplitude appears in NM, with peak-to-
318 valley difference up to 13.5 ppm. SW, SM, SE, and MC have similar amplitudes of 7-8 ppm, smaller than the other
319 three regions. To evaluate the performance of CT2015 on column ΔXCO_2 , CT2015 results are sampled to match the
320 latitude, longitude, altitude and time of actual measurements. Note that aircraft profiles are not assimilated in
321 CT2015, so aircraft data are independent of the CT2015 data assimilation. Figure 7b shows monthly partial columns
322 of ΔXCO_2 calculated from CT2015, which demonstrate good agreement with results from measurements. Only
323 small seasonal biases exist in CT2015, with high bias occurring mostly in spring and early summer and low bias in
324 September and October (Fig. S4). The overall differences of monthly partial column ΔXCO_2 (CT2015 -
325 measurements) mainly fall in the range of -0.64 ppm (5th percentile) to 0.84 ppm (95th percentile) with a mean
326 difference of 0.13 ppm. These differences are of similar magnitude to the uncertainties of partial column ΔXCO_2
327 calculated from the measurements (Fig. S5). It is clear that CT2015 captures the long-term mean variations of both
328 phase and amplitude of partial column XCO_2 reasonably well when compared with well-calibrated measurements
329 across North America.
330

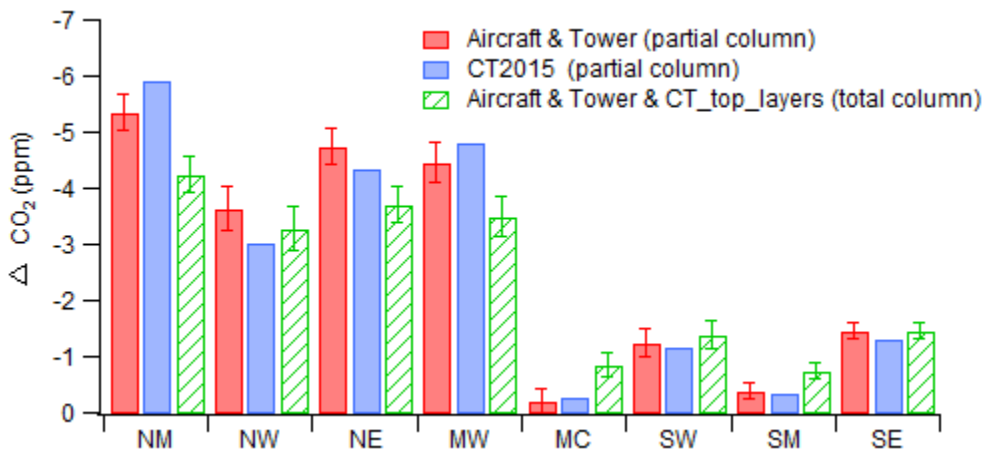


331
332 **Fig. 7.** (a). Partial column ΔXCO_2 calculated from aircraft and tower data; (b). Partial column ΔXCO_2 calculated
333 from CT2015; (c). Total column ΔXCO_2 calculated from aircraft and tower data and including the top layer data
334 from CT2015.

335

336 Total column ΔXCO_2 is presented in Fig. 7c. In regions NW, NM, NE, and MW, seasonal variations of total
337 column ΔXCO_2 are very similar in both phase and amplitude (8-9 ppm peak to valley). For SW, SM, SE, and MC,
338 amplitudes are ~5.5 ppm. The smallest spatial gradients occur during May and October, which result in maximum
339 differences among all regions of only 0.9 and 0.7 ppm, respectively. The largest spatial gradients occur during June,
340 July and August, which result in maximum differences of 2.4, 4.5, and 4.1 ppm, respectively. It is interesting that the
341 deepest seasonal drawdown is seen in region NM, not in region MW that encompasses the very intensive

342 agricultural activities in the U.S. mid-west, which suggest the possibility of strong upwind influence in the NM
 343 region. Transported signals have significant influences on total column ΔXCO_2 . The summer total column ΔXCO_2 ,
 344 represented by the June to August average from CT2015, has a magnitude that is similar to observations with
 345 differences no more than 1 ppm (Fig. 8). Based on the seasonal patterns of total column ΔXCO_2 (Fig. 7c) and the
 346 summer column ΔXCO_2 (Fig. 8), we can separate the eight regions into two groups. The group with NW, NM, NE,
 347 and MW, has ~ 3 ppm stronger drawdown (larger amplitude) than the group with SW, SM, SE, and MC. For winter
 348 total column ΔXCO_2 (December to February average), the maximum spatial difference is only 1.6 ppm, with the
 349 highest total column ΔXCO_2 of 1.2 ppm in NE and the lowest value of -0.3 ppm in MC.
 350



351
 352 **Fig. 8.** Long-term mean (2004-2014) June to August partial and total column ΔXCO_2 . Error bars represent one
 353 standard deviation from the bootstrap uncertainty calculation (see Sect. 2.3).
 354

355 3.4 Influence of large scale circulation

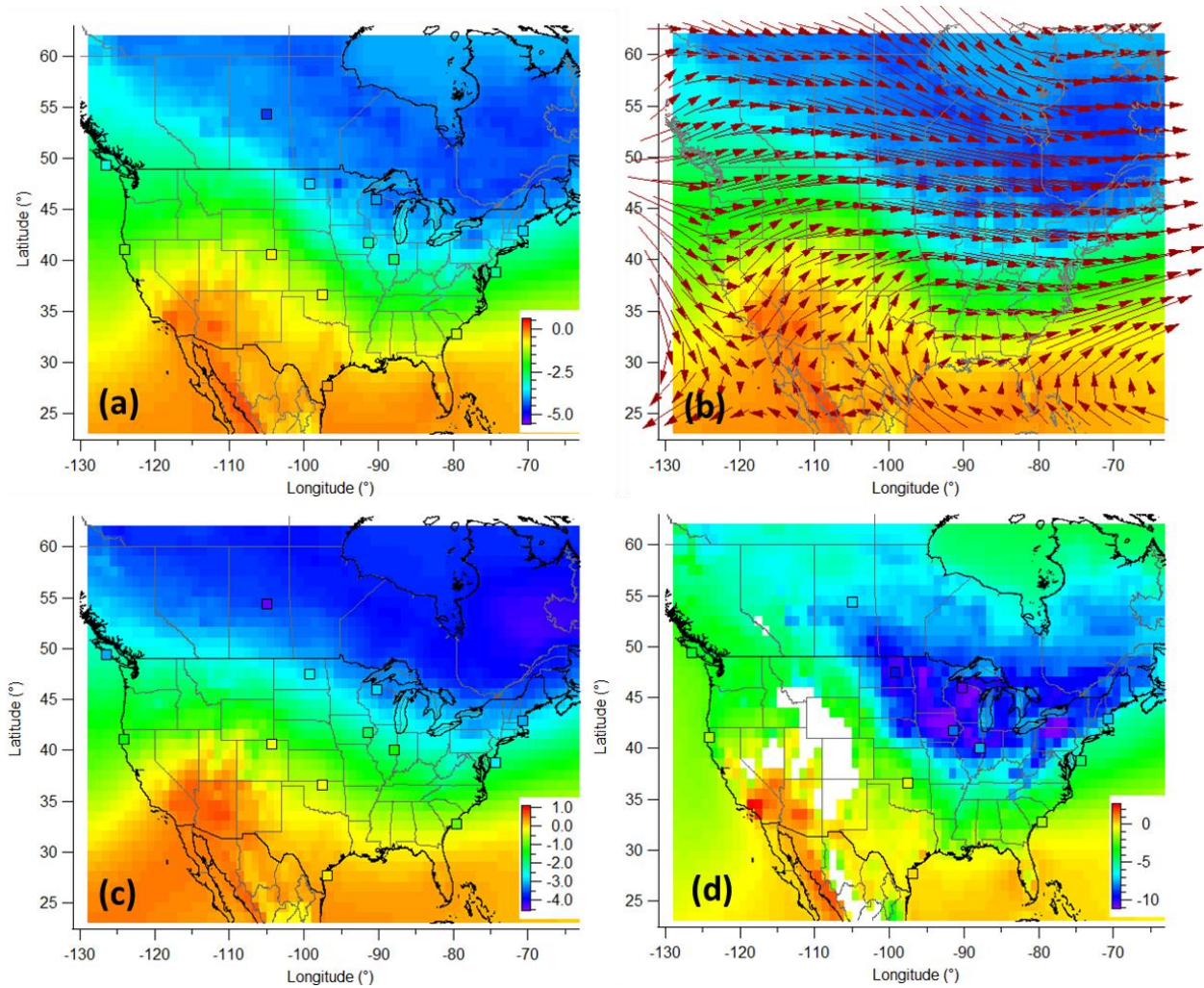
356 Figure 9 shows long-term mean summer column ΔXCO_2 calculated from CT2015, together with full column
 357 ΔXCO_2 from individual aircraft sites. Note that some aircraft sites have less than 11 years of data that CT2015
 358 shows in Fig. 9, only aircraft sites with more than 6 years of data are presented, the actual values are provided in
 359 Table S2. The fact that total column ΔXCO_2 from CT2015 agrees well with aircraft sites supports the performance
 360 of CT2015 on a long-term average basis. The observations show a similar summer spatial pattern, with lower
 361 column ΔXCO_2 in the north and northeast regions and higher column ΔXCO_2 in the south and southwest regions
 362 (Fig. 9a). Scattered hot spots of high column ΔXCO_2 associated with surface emissions from megacities, or cold
 363 spots associated with strong local uptake, are not or just barely visible in the long-term average column ΔXCO_2 map
 364 at $1^\circ \times 1^\circ$ resolution. Instead, the wave-like pattern of column ΔXCO_2 over North America reflects the average large
 365 scale circulation. To support our hypothesis on the influence of large scale circulation, we analyze the long term
 366 mean wind pattern over North America. We can see that air masses from northwest of the continent bring in low
 367 average column ΔXCO_2 , while air masses from the south (mainly the subtropical Pacific Ocean and the Gulf of

368 Mexico) bring in high column ΔXCO_2 (Fig. 9b). The zonal gradients over the continent, especially north of $40^\circ N$,
369 also reflect long-term average wind patterns; southwest wind corresponds to higher column ΔXCO_2 over the western
370 part of the continent until the wind direction shifts to west-northwest over the eastern part of the continent. This
371 wind pattern matches well with the geographic division of the over/under -3 ppm areas colored in green/blue in the
372 column ΔXCO_2 map (Fig. 9b). Figure 9c and 9d shows partial column averages for free troposphere (800-330 hPa)
373 and lower troposphere (below 800 hPa), respectively. The free troposphere spatial gradient also demonstrates a
374 wave-like pattern. A previous study on the total column CO_2 from ground based Total Carbon Column Observation
375 Network (TCCON) found strong correlation between the mid-latitude column CO_2 and synoptic-scale variation of
376 potential temperature (θ , at 700 hPa), a dynamic tracer for adiabatic air transport (Keppel-Aleks et al., 2012). Thus
377 they also propose that the variations in column CO_2 are mainly driven by large-scale flux and transport. Analysis of
378 the interannual variability of the seasonal cycle amplitudes of column CO_2 in North Hemisphere has also found
379 significant contribution of large-scale circulations to the north-south gradient (Wunch et al., 2013).

380 The strong drawdown over northeast North America in summer is a consequence of long-range transport of low
381 CO_2 from northeast Eurasia, in addition to regional terrestrial uptake. Sweeney et al. (2015) notes well-mixed
382 vertical profiles (up to 8 km) of CO_2 , CO, CH_4 , N_2O , and SF_6 from THD, ESP and PFA (Poker Flat, Alaska; 65.07° ,
383 -147.29°) sites and suggests that air coming across the Pacific was strongly influenced by Asian surface fluxes
384 before being vertically homogenized as it passed over the Pacific Ocean. This well-mixed air forms an important
385 boundary condition in the column CO_2 of air coming into the North American continent. This was best illustrated at
386 sites like PFA where the summertime minimum in CO_2 significantly preceded maximum ecosystem uptake of CO_2 ,
387 implying significant influence of transported air from lower latitude regions from Asia. We further conduct an
388 experiment using Carbon Tracker to investigate the importance of this effect. A control run and a “masked run” are
389 conducted for 2010-2012, in which the Eurasian boreal flux is turned on/off. The MLO CO_2 trend from each model
390 scenario is used as reference background and thus removed before total column ΔXCO_2 calculation. Figure 10 shows
391 the results for 2012 summer, which is an average summer when compared with the 2004-2014 mean pattern (Fig. 9
392 and Fig. 11). The maximum north-south difference reduces to ~ 2.5 ppm after we turn off the Eurasian boreal flux,
393 compared with ~ 5 ppm from the control run. In both control and masked scenarios, the free troposphere partial
394 ΔXCO_2 demonstrates similar spatial patterns as for total column ΔXCO_2 (Fig. S6). This result combined with results
395 from Sweeney et al. (2015) demonstrates that the transport of low CO_2 resulting from large summertime Eurasian
396 boreal uptake has a large contribution on the overall summer total column CO_2 decrease in North America.

397

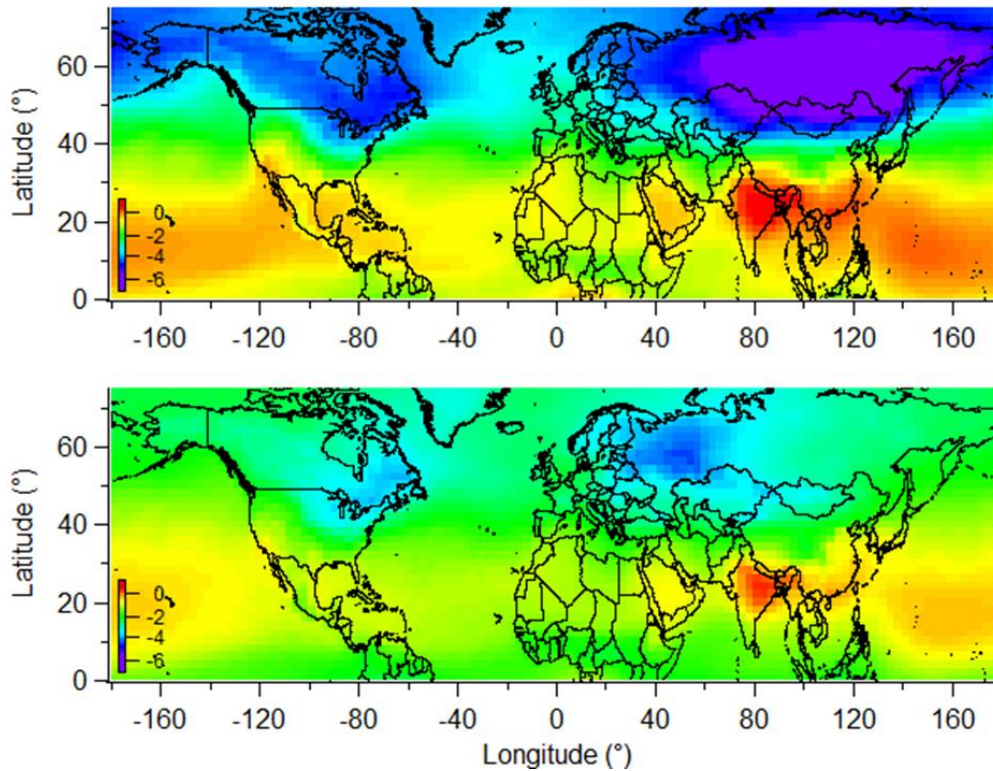
398



399

400 **Fig. 9.** Long-term mean (2004-2014) June-August total column ΔXCO_2 from CT2015 in $1^\circ \times 1^\circ$ spatial resolution
 401 with total column ΔXCO_2 for 13 individual aircraft sites in squares (a), and CT2015 column ΔXCO_2 overlaid with
 402 pressure-weighted (1000 hPa to 500 hPa) mean wind vectors for the same period (b). (c) and (d) are similar as (a),
 403 except for free troposphere (800 to 330 hPa) and lower troposphere (below 800 hPa), respectively. Note the different
 404 color scales.

405



406

407 **Fig. 10.** Total column ΔXCO_2 from Carbon Tracker control (top panel) and masked (bottom panel, Eurasian boreal
 408 flux is masked) runs for 2012 June-August ($3^\circ \times 2^\circ$ spatial resolution). MLO trend from each individual scenario is
 409 removed before the ΔXCO_2 calculation. Same color scale is used as in Fig. 9a. Partial column ΔXCO_2 patterns for
 410 free troposphere (800 to 330 hPa) and lower troposphere (below 800 hPa) are provided in SI.

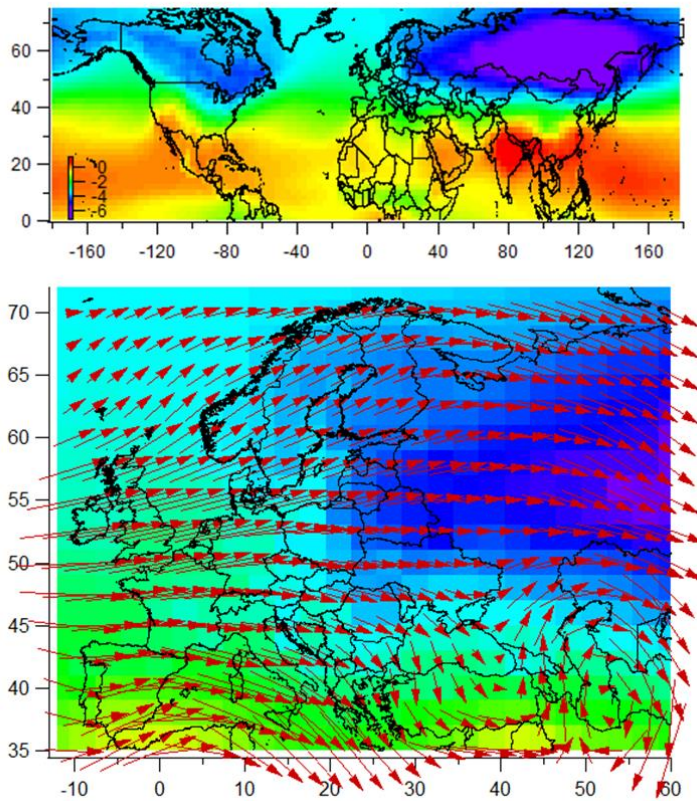
411 3.5 A comparison with apparent gradients over Europe

412 Figure 11 shows the climatological June - August mean modeled global column ΔXCO_2 map in $3^\circ \times 2^\circ$ spatial
 413 resolution, which presents smooth wave-like patterns. Reuter et al. (2014) use SCIAMACHY and GOSAT satellite
 414 retrievals of column CO_2 and inverse modelling to infer a very large net CO_2 uptake flux over European region.
 415 Column ΔXCO_2 from CT2015 (Fig. 11) exhibits a drastically different summer spatial pattern over Europe
 416 compared with the eight year mean (2003-2010) June through August satellite retrievals presented by Reuter et al.
 417 (2014, their Fig. 2a). The spatial gradient from CT2015 results in a maximum 3-4 ppm difference and a gradual
 418 pattern, instead of as much as 6 ppm from satellite retrievals. There is no sign of XCO_2 hot spots from surface
 419 emissions or removals in the CT2015 spatial pattern over Europe (Fig. 11), in contrast to several hot spots that are
 420 apparent from the 8-year averaged SCIAMACHY satellite retrievals over Ireland, U.K., Belgium, Netherland, north
 421 of Germany, and south of Sweden, and low spots over the Ukraine and Kazakhstan (Reuter et al., 2014). This
 422 SCIAMACHY retrieval pattern contradicts our understanding of the significant influence of large-scale transport on
 423 column ΔXCO_2 . Although the NOAA/ESRL CT2015 (<https://www.esrl.noaa.gov/gmd/ccgg/carbontracker/CT2015/>)
 424 assimilates fewer observations over Europe than Carbon Tracker Europe (<http://www.carbontracker.eu/>), both

425 models produced similar fluxes over the European region (see both websites for detailed fluxes). The $3^{\circ} \times 2^{\circ}$ grid
426 from CT2015 is not likely responsible for a much smoother pattern for Carbon Tracker, compared with the $2^{\circ} \times 2^{\circ}$
427 grid from satellite retrievals (Reuter et al., 2014) . The North America region on the $3^{\circ} \times 2^{\circ}$ grid in Fig. 11 shows
428 similar pattern as the $1^{\circ} \times 1^{\circ}$ grid in Fig. 9, with similar spatial difference of ~ 5 ppm. A smoother spatial
429 distribution should be expected in Europe for the long-term mean column XCO_2 (Fig. 11) due to the influences of
430 dominating west and southwest winds in summer. We have also evaluated the importance of sampling bias by
431 sampling CT2015 at the same latitude/longitude/hour (within 1 hour) as in SCIAMACHY BESD (v02.00.08) data
432 (Reuter et al., 2011). The 8-year mean pattern shows much smaller gradients (3-4 ppm maximum) without
433 significant hot/cold spots at those locations as SCIAMACHY (Fig. S7). Sampling bias is unlikely the main reason
434 for the unphysical column XCO_2 spatial pattern from SCIAMACHY. Since the satellite retrievals in Reuter et al.
435 (2014) appear to show unrealistic column XCO_2 spatial gradients over Europe, they should not be used to derive any
436 estimates of a European carbon sink. A recent study (Feng et al., 2016) using inverse modeling suggests that satellite
437 retrievals outside the immediate European region and a small bias of only 0.5 ppm were sufficient to produce the
438 apparent large carbon sink in the study of Reuter et al. (2014). This is expected from elementary mass balance
439 considerations as in Sec.1 above. Spatial gradients are the fundamental signals to infer regional fluxes. Since spatial
440 gradients from CT2015 are realistic, boreal fluxes inferred by CT2015, should be more trustworthy than fluxes
441 estimated based on unrealistic spatial pattern. However, the European carbon sink is still inconclusive; the
442 discrepancies among different methods and results are further discussed by Reuter et al. (2017). Increasing the
443 amount of highly precise observations such as the well-calibrated surface measurements and vertical profiles can
444 greatly help to estimate the carbon sink.

445

446



447

448 **Fig. 11.** Long-term mean (2004-2014) June - August total column ΔXCO_2 from CT2015 (top panel) in $3^\circ \times 2^\circ$
 449 spatial resolution, and detail for Europe overlaid with pressure-weighted (1000 hPa to 500 hPa) mean wind
 450 vectors for the same period (bottom panel). The color scale is the same as in Fig. 9a, which is scaled to reflect 6
 451 ppm difference of XCO_2 to compare with satellite retrievals from Reuter et al. (their Fig. 2a, 2014).

452 **4 Conclusion**

453 Aircraft and tall tower measurements from the NOAA GGGRN provide detailed information describing the long-
 454 term average temporal and spatial variations of CO_2 in the PBL and the free troposphere. These data provide
 455 valuable constraints for evaluating model simulations and satellite retrievals. Seasonal cycle peak-to-peak
 456 amplitudes of CO_2 are largest below 2 km, where those maximum values are about twice those in the vertical layers
 457 above, indicating that most of the information on surface sources and sinks resides in the continental PBL. Large
 458 spatial gradients of CO_2 over North America are observed below 2 km during summer (with maximum difference of
 459 ~ 15.5 ppm between MW and SM), while higher altitude data (above 2 km) have much smaller contributions to
 460 spatial gradients, with a maximum difference of 4 ppm. The spatial differences of CO_2 in the upper troposphere and
 461 above (330 hPa to 0 hPa) are less than 0.5 ppm, according to CT2015. Comparison with Aircore measurements
 462 shows CT2015 performs well simulating upper tropospheric and lower stratospheric patterns.

463 Our long-term mean vertical profiles show that tower data agree well with aircraft data at similar vertical levels.
 464 Partial column ΔXCO_2 was calculated from the long-term mean vertical profiles. By comparing the partial column

465 ΔXCO_2 from measurements with those from CT2015, we verify that CT2015 captures the long-term mean patterns
466 of both phase and amplitude of partial ΔXCO_2 .

467 Large spatial gradients of ΔXCO_2 only appeared in summer, during which time the north and northeast regions
468 had ~ 3 ppm stronger drawdowns than the south and southwest regions. Scattered hot spots of high column ΔXCO_2
469 associated with surface emissions from megacities, or cold spots associated with strong local uptake, are not or just
470 barely visible in the long-term average column ΔXCO_2 . Instead, the wave-like pattern of column ΔXCO_2 over North
471 America matches well with the average large scale circulation. A CarbonTracker experiment to investigate the
472 impact of Eurasian long-range transport suggests that the large summer time Eurasian boreal flux alone contributes
473 about half of the north-south column ΔXCO_2 gradient across North America. Considering the transported signals
474 from other upwind regions, including northern Canada, we expect that the transported signals have the overall
475 largest contribution to the total column ΔXCO_2 spatial gradient.

476 **Author contributions**

477 Xin Lan was responsible for study design, data analysis, and manuscript writing. Pieter Tans was responsible for
478 study design, data analysis, and manuscript improvement. Colm Sweeney and Arlyn Andrews provided
479 measurement data and improved manuscript. Andrew Jacobson provided modelled data and improved manuscript.
480 Edward Dlugokencky analyzed measurements and ensured data quality, and improved manuscript. Jonathan Kofler
481 conducted tower measurements and improved manuscript. Molly Crotwell, Patricia Lang, and Sonja Wolter
482 analyzed measurements and ensured data quality. Kirk Thoning provided data smoothing method.

483 **Acknowledgements**

484 We especially thank John Mund for extracting NARR meteorological variables for our measurements. This
485 research was supported by a fellowship from the National Research Council Research Associateship Programs.

486 **References**

487 Andrews, A. E., Kofler, J. D., Trudeau, M. E., Williams, J. C., Neff, D. H., Masarie, K. A., Chao, D. Y., Kitzis, D.
488 R., Novelli, P. C., Zhao, C. L., Dlugokencky, E. J., Lang, P. M., Crotwell, M. J., Fischer, M. L., Parker, M. J.,
489 Lee, J. T., Baumann, D. D., Desai, A. R., Stanier, C. O., De Wekker, S. F. J., Wolfe, D. E., Munger, J. W. and
490 Tans, P. P.: CO₂, CO, and CH₄ measurements from tall towers in the NOAA Earth System Research
491 Laboratory's Global Greenhouse Gas Reference Network: instrumentation, uncertainty analysis, and
492 recommendations for future high-accuracy greenhouse gas monitoring efforts, *Atmos. Meas. Tech.*, 7, 647-687,
493 2014.

494 Banta, R. M., Senff, C. J., Nielsen-Gammon, J., Darby, L. S., Ryerson, T. B., Alvarez, R. J., Sandberg, S. R.,
495 Williams, E. J. and Trainer, M.: A bad air day in Houston', *B. Am. Meteorol. Soc.*, 86, 657, DOI:
496 <http://dx.doi.org/10.1175/BAMS-86-5-657>, 2005.

497 Biraud, S. C., Torn, M. S., Smith, J. R., Sweeney, C., Riley, W. J. and Tans, P. P.: A multi-year record of airborne
498 CO₂ observations in the US Southern Great Plains, *Atmos. Meas. Tech.*, 6, 751-763, 2013.

499 Buchwitz, M., Reuter, M., Bovensmann, H., Pillai, D., Heymann, J., Schneising, O., Rozanov, V., Krings, T.,
500 Burrows, J. P., Boesch, H., Gerbig, C., Meijer, Y. and Loscher, A. : Carbon Monitoring Satellite (CarbonSat):
501 assessment of atmospheric CO₂ and CH₄ retrieval errors by error parameterization, *Atmos. Meas. Tech.*, 6,
502 3477-3500, 2013.

503 Chevallier, F., Breon, F. M. and Rayner, P. J.: Contribution of the Orbiting Carbon Observatory to the estimation of
504 CO₂ sources and sinks: Theoretical study in a variational data assimilation framework, *J. Geophys. Res.*
505 *Atmos.*, 112, D09307, doi:10.1029/2006JD007375, 2007.

506 Choi, Y. H., Vay, S. A., Vadrevu, K. P., Soja, A. J., Woo, J. H., Nolf, S. R., Sachse, G. W., Diskin, G. S., Blake, D.
507 R., Blake, N. J., Singh, H. B., Avery, M. A., Fried, A., Pfister, L. and Fuelberg, H. E.: Characteristics of the
508 atmospheric CO₂ signal as observed over the conterminous United States during INTEX-NA, *J. Geophys. Res.*
509 *Atmos.*, 113, D07301, doi:10.1029/2007JD008899, 2008.

510 Ciais, P., Rayner, P., Chevallier, F., Bousquet, P., Logan, M., Peylin, P. and Ramonet, M.: Atmospheric inversions
511 for estimating CO₂ fluxes: methods and perspectives, *Climatic Change*, 103, 69-92, 2010.

512 Conway, T. J., Tans, P. P., Waterman, L. S. and Thoning, K. W.: Evidence for interannual variability of the carbon-
513 cycle from the national-oceanic-and-atmospheric-administration climate-monitoring-and-diagnostics-laboratory
514 global-air-sampling-network, *J. Geophys. Res. Atmos.*, 99, 22831-22855, 1994.

515 Crevoisier, C., Sweeney, C., Gloor, M., Sarmiento, J. L. and Tans, P. P.: Regional US carbon sinks from three-
516 dimensional atmospheric CO₂ sampling, *Proc. Natl. Acad. Sci. U. S. A.*, 107, 18348-18353, 2010.

517 Crisp, D., Fisher, B. M., O'Dell, C., Frankenberg, C., Basilio, R., Bosch, H., Brown, L. R., Castano, R., Connor, B.,
518 Deutscher, N. M., Eldering, A., Griffith, D., Gunson, M., Kuze, A., Mandrake, L., McDuffie, J.,
519 Messerschmidt, J., Miller, C. E., Morino, I., Natraj, V., Notholt, J., O'Brien, D. M., Oyafuso, F., Polonsky, I.,
520 Robinson, J., Salawitch, R., Sherlock, V., Smyth, M., Suto, H., Taylor, T. E., Thompson, D. R., Wennberg, P.
521 O., Wunch, D., and Yung, Y. L.: The ACOS CO₂ retrieval algorithm – Part II: Global XCO₂ data
522 characterization, *Atmos. Meas. Tech.*, 5, 687–707, doi:10.5194/amt-5-687-2012, 2012.

523 Dee, D. P., Uppala, S. M., Simmons, A. J., Berrisford, P., Poli, P., Kobayashi, S., Andrae, U., Balmaseda, M. A.,
524 Balsamo, G., Bauer, P., Bechtold, P., Beljaars, A. C. M., van de Berg, L., Bidlot, J., Bormann, N., Delsol, C.,
525 Dragani, R., Fuentes, M., Geer, A. J., Haimberger, L., Healy, S. B., Hersbach, H., Holm, E. V., Isaksen, L.,
526 Kallberg, P., Kohler, M., Matricardi, M., McNally, A. P., Monge-Sanz, B. M., Morcrette, J. J., Park, B. K.,
527 Peubey, C., de Rosnay, P., Tavolato, C., Thepaut, J. N. and Vitart, F.: The ERA-Interim reanalysis:
528 configuration and performance of the data assimilation system, *Q.J.R. Meteorol. Soc.*, 137, 553-597, 2011.

529 Denning, A. S., Takahashi, T., and Friedlingstein, P.: Can a strong atmospheric CO₂ rectifier effect be reconciled
530 with a “reasonable” carbon budget?, *Tellus B*, 51, 249–253, 1999.

531 Feng, L., Palmer, P. I., Parker, R. J., Deutscher, N. M., Feist, D. G., Kivi, R., Morino, I. and Sussmann, R.:
532 Estimates of European uptake of CO₂ inferred from GOSAT X-CO₂ retrievals: sensitivity to measurement bias
533 inside and outside Europe, *Atmos. Chem. Phys.*, 16, 1289-1302, 2016.

534 Frankenberg, C., Kulawik, S. S., Wofsy, S., Chevallier, F., Daube, B., Kort, E. A., O'Dell, C., Olsen, E. T., and
535 Osterman, G.: Using airborne HIAPER Pole-to-Pole Observations (HIPPO) to evaluate model and remote
536 sensing estimates of atmospheric carbon dioxide, *Atmos. Chem. Phys.*, , 16, 7867–7878, 2016. doi:10.5194/acp-
537 16-7867-2016, 2016.

538 Gerbig, C., Lin, J. C., Wofsy, S. C., Daube, B. C., Andrews, A. E., Stephens, B. B., Bakwin, P. S. and Grainger, C.
539 A.: Toward constraining regional-scale fluxes of CO₂ with atmospheric observations over a continent: 1.
540 Observed spatial variability from airborne platforms *J. Geophys. Res. Atmos.*, 108, doi:10.1029/2002JD003018,
541 2003.

542 Chevallier, F., Palmer, P. I., Feng, L., Boesch, H., O'Dell, C. W., and Bousquet, P.: Towards robust and consistent
543 regional CO₂ flux estimates from in situ and space-borne measurements of atmospheric CO₂, *Geophys. Res.*
544 *Let.*, 41, 1065–1070, doi:10.1002/2013GL058772, 2014.

545 Gourdji, S. M., Mueller, K. L., Yadav, V., Huntzinger, D. N., Andrews, A. E., Trudeau, M., Petron, G., Nehrkorn,
546 T., Eluszkiewicz, J., Henderson, J., Wen, D., Lin, J., Fischer, M., Sweeney, C. and Michalak, A. M.: North
547 American CO₂ exchange: inter-comparison of modeled estimates with results from a fine-scale atmospheric
548 inversion, *Biogeosci.*, 9, 457-475, 2012

549 Gurney, K. R., Law, R. M., Denning, A. S., Rayner, P. J., Baker, D., Bousquet, P., Bruhwiler, L., Chen, Y. H., Ciais,
550 P., Fan, S., Fung, I. Y., Gloor, M., Heimann, M., Higuchi, K., John, J., Maki, T., Maksyutov, S., Masarie, K.,
551 Peylin, P., Prather, M., Pak, B. C., Randerson, J., Sarmiento, J., Taguchi, S., Takahashi, T. and Yuen, C. W.:
552 Towards robust regional estimates of CO₂ sources and sinks using atmospheric transport models, *Nature*,
553 415(6872), 626-630, 2002.

554 Gurney, K. R., Law, R. M., Denning, A. S., Rayner, P. J., Pak, B. C., Baker, D., Bousquet, P., Bruhwiler, L., Chen,
555 Y. H., Ciais, P., Fung, I. Y., Heimann, M., John, J., Maki, T., Maksyutov, S., Peylin, P., Prather, M. and
556 Taguchi, S.: Transcom 3 inversion intercomparison: Model mean results for the estimation of seasonal carbon
557 sources and sinks, *Global Biogeochem. Cycles*, 18, GB1010, doi:10.1029/2003GB002111, 2004.

558 Houweling, S., Breon, F. M., Aben, I., Rodenbeck, C., Gloor, M., Heimann, M. and Ciais, P.: Inverse modeling of
559 CO₂ sources and sinks using satellite data: a synthetic inter-comparison of measurement techniques and their
560 performance as a function of space and time, *Atmos. Chem. Phys.*, 4, 523-538, 2004.

561 Inoue, M., Morino, I., Uchino, O., Miyamoto, Y., Yoshida, Y., Yokota, T., Machida, T., Sawa, Y., Matsueda, H.,
562 Sweeney, C., Tans, P. P., Andrews, A. E., Biraud, S. C., Tanaka, T., Kawakami, S. and Patra, P. K.: Validation
563 of XCO₂ derived from SWIR spectra of GOSAT TANSO-FTS with aircraft measurement data, *Atmos. Chem.*
564 *Phys.*, 13, 9771-9788, 2013.

565 Inoue, M., Morino, I., Uchino, O., Nakatsuru, T., Yoshida, Y., Yokota, T., Wunch, D., Wennberg, P. O., Roehl, C.
566 M., Griffith, D. W. T., Velazco, V. A., Deutscher, N. M., Warneke, T., Notholt, J., Robinson, J., Sherlock, V.,
567 Hase, F., Blumenstock, T., Rettinger, M., Sussmann, R., Kyrö, E., Kivi, R., Shiomi, K., Kawakami, S., De
568 Mazière, M., Arnold, S. G., Feist, D. G., Barrow, E. A., Barney, J., Dubey, M., Schneider, M., Iraci, L.,
569 Podolske, J. R., Hillyard, P., Machida, T., Sawa, Y., Tsuboi, K., Matsueda, H., Sweeney, C., Tans, P. P.,
570 Andrews, A. E., Biraud, S. C., Fukuyama, Y., Pittman, J. V., Kort, E. A., and Tanaka, T.: Bias corrections of

571 GOSAT SWIR XCO₂ and XCH₄ with TCCON data and their evaluation using aircraft measurement data,
572 Atmos. Meas. Tech. 9, 3491–3512, 2016, doi:10.5194/amt-9-3491-2016.

573 Karion, A., Sweeney, C., Tans, P., and Newberger, T.: AirCore: An Innovative Atmospheric Sampling System, J.
574 Atmos. Ocean. Tech., 27, 1839–1853, doi:10.1175/2010JTECHA1448.1, 2010.

575 Karion, A., C. Sweeney, S. Wolter, T. Newberger, H. Chen, A. Andrews, J. Kofler, D. Neff, and P. Tans (2013),
576 Long-term greenhouse gas measurements from aircraft, Atmos. Meas. Tech., 6(3), 511–526, doi:10.5194/amt-6-
577 511-2013.

578 Keeling, C. D. and Rakestraw, N. W.: The concentration of carbon dioxide in the atmosphere, J. Geophys. Res., 65,
579 2502-2502, 1960.

580 Keppel-Aleks, G., Wennberg, P. O., Washenfelder, R. A., Wunch, D., Schneider, T., Toon, G. C., Andres, R. J.,
581 Blavier, J.-F., Connor, B., Davis, K. J., Desai, A. R., Messerschmidt, J., Notholt, J., Roehl, C. M., Sherlock, V.,
582 Stephens, B. B., Vay, S. A., and Wofsy, S. C.: The imprint of surface fluxes and transport on variations in total
583 column carbon dioxide, Biogeosci., 9, 875– 891, doi:10.5194/bg-9-875-2012, 2012.

584 Kulawik, S. S., Worden, J. R., Wofsy, S. C., Biraud, S. C., Nassar, R., Jones, D. B. A., Olsen, E. T., Jimenez, R.,
585 Park, S., Santoni, G. W., Daube, B. C., Pittman, J. V., Stephens, B. B., Kort, E. A., Osterman, G. B. and Team,
586 T. E. S.: Comparison of improved Aura Tropospheric Emission Spectrometer CO₂ with HIPPO and SGP
587 aircraft profile measurements, Atmos. Chem. Phys., 13, 3205-3225, 2013.

588 Lauvaux, T., Schuh, A. E., Uliasz, M., Richardson, S., Miles, N., Andrews, A. E., Sweeney, C., Diaz, L. I., Martins,
589 D., Shepson, P. B. and Davis, K. J.: Constraining the CO₂ budget of the corn belt: exploring uncertainties from
590 the assumptions in a mesoscale inverse system, Atmos. Chem. Phys., 12, 337-354, 2012.

591 Machida, T., Kita, K., Kondo, Y., Blake, D., Kawakami, S., Inoue, G. and Ogawa, T. : Vertical and meridional
592 distributions of the atmospheric CO₂ mixing ratio between northern midlatitudes and southern subtropics, J.
593 Geophys. Res. Atmos., 108(D3), 8401, doi:10.1029/2001JD000910, 2002.

594 Machida, T., Matsueda, H., Sawa, Y., Nakagawa, Y., Hirokuni, K., Kondo, N., Goto, K., Nakazawa, T., Ishikawa, K.
595 and Ogawa, T.: Worldwide Measurements of Atmospheric CO₂ and Other Trace Gas Species Using
596 Commercial Airlines, J. Atmos. Ocean. Tech., 25(10), 1744-1754, 2008.

597 Mesinger, F., DiMego, G., Kalnay, E., Mitchell, K., Shafran, P. C., Ebisuzaki, W., Jovic, D., Woollen, J., Rogers,
598 E., Berbery, E. H., Ek, M. B., Fan, Y., Grumbine, R., Higgins, W., Li, H., Lin, Y., Manikin, G., Parrish, D., and
599 Shi, W.: North American regional reanalysis, B. Am. Meteorol. Soc., 87, 343–360, doi:10.1175/BAMS-87-3-
600 343, 2006.

601 Messerschmidt, J., Geibel, M. C., Blumenstock, T., Chen, H., Deutscher, N. M., Engel, A., Feist, D. G., Gerbig, C.,
602 Gisi, M., Hase, F., Katrynski, K., Kolle, O., Lavric, J. V., Notholt, J., Palm, M., Ramonet, M., Rettinger, M.,
603 Schmidt, M., Sussmann, R., Toon, G. C., Truong, F., Warneke, T., Wennberg, P. O., Wunch, D. and Xueref-
604 Remy, I.: Calibration of TCCON column-averaged CO₂: the first aircraft campaign over European TCCON
605 sites, Atmos. Chem. Phys., 11(21), 10765-10777, 2011.

606 Miller, C. E., Crisp, D., DeCola, P. L., Olsen, S. C., Randerson, J. T., Michalak, A. M., Alkhaled, A., Rayner, P.,
607 Jacob, D. J., Suntharalingam, P., Jones, D. B. A., Denning, A. S., Nicholls, M. E., Doney, S. C., Pawson, S.,

608 Boesch, H., Connor, B. J., Fung, I. Y., O'Brien, D., Salawitch, R. J., Sander, S. P., Sen, B., Tans, P., Toon, G.
609 C., Wennberg, P. O., Wofsy, S. C., Yung, Y. L. and Law, R. M.: Precision requirements for space-based X-CO₂
610 data, *J. Geophys. Res. Atmos.*, 112, D10314, doi:10.1029/2006JD007659, 2007.

611 Miller, J. B., Lehman, S. J., Montzka, S. A., Sweeney, C., Miller, B. R., Karion, A., Wolak, C., Dlugokencky, J.,
612 Southon, J., Turnbull, J. C., and Tans, P. P.: Linking emissions of fossil fuel CO₂ and other anthropogenic trace
613 gases using atmospheric ¹⁴C, *J. Geophys. Res.*, 117, D08302, doi:10.1029/2011JD017048, 2012.

614 Miller, S. T. K., Keim, B. D., Talbot, R. W. and Mao, H.: Sea breeze: Structure, forecasting, and impacts, *Rev.*
615 *Geophys.*, 41, 1011, doi:10.1029/2003RG000124, 2003.

616 Miyamoto, Y., Inoue, M., Morino, I., Uchino, O., Yokota, T., Machida, T., Sawa, Y., Matsueda, H., Sweeney, C.,
617 Tans, P. P., Andrews, A. E. and Patra, P. K.: Atmospheric column-averaged mole fractions of carbon dioxide at
618 53 aircraft measurement sites, *Atmos. Chem. Phys.*, 13(10), 5265-5275, 2013.

619 Peters, W., Jacobson, A. R., Sweeney, C., Andrews, A. E., Conway, T. J., Masarie, K., Miller, J. B., Bruhwiler, L.
620 M. P., Petron, G., Hirsch, A. I., Worthy, D. E. J., van der Werf, G. R., Randerson, J. T., Wennberg, P. O., Krol,
621 M. C. and Tans, P. P.: An atmospheric perspective on North American carbon dioxide exchange:
622 CarbonTracker, *Proc. Natl. Acad. Sci. U. S. A.*, 104(48), 18925-18930, 2007.

623 Ramonet, M., Ciais, P., Nepomniachii, I., Sidorov, K., Neubert, R. E. M., Langendorfer, U., Picard, D., Kazan, V.,
624 Biraud, S., Gusti, M., Kolle, O., Schulze, E. D. and Lloyd, J.: Three years of aircraft-based trace gas
625 measurements over the Fyodorovskoye southern taiga forest, 300 km north-west of Moscow, *Tellus B-Chem.*
626 *Phys. Meteor.*, 54(5), 713-734, 2002.

627 Reuter, M., Bovensmann, H., Buchwitz, M., Burrows, J. P., Connor, B. J., Deutscher, N. M., Griffith, D. W. T.,
628 Heymann, J., Keppel-Aleks, G., Messerschmidt, J., Notholt, J., Petri, C., Robinson, J., Schneising, O., Sherlock,
629 V., Velasco, V., Warneke, T., Wennberg, P. O. and Wunch, D.: Retrieval of atmospheric CO₂ with enhanced
630 accuracy and precision from SCIAMACHY: Validation with FTS measurements and comparison with model
631 results, *J. Geophys. Res. Atmos.*, 116, 2011.

632 Reuter, M., Buchwitz, M., Hilker, M., Heymann, J., Schneising, O., Pillai, D., Bovensmann, H., Burrows, J. P.,
633 Bosch, H., Parker, R., Butz, A., Hasekamp, O., O'Dell, C. W., Yoshida, Y., Gerbig, C., Nehrkorn, T.,
634 Deutscher, N. M., Warneke, T., Notholt, J., Hase, F., Kivi, R., Sussmann, R., Machida, T., Matsueda, H. and
635 Sawa, Y.: Satellite-inferred European carbon sink larger than expected, *Atmos. Chem. Phys.*, 14(24), 13739-
636 13753, 2014.

637 Reuter, M., Buchwitz, M., Hilker, M., Heymann, J., Bovensmann, H., Burrows, J. P., Houweling, S., Liu, Y. Y.,
638 Nassar, F., Chevallier, F., Ciais, P., Marshall, J., and Reichstein, M.: How much CO₂ is taken up by the
639 European terrestrial biosphere? *Bull. Am. Meteor. Soc.*, 98, 665–671, doi:10.1175/BAMS-D-15-00310.1, 2017.

640 Saitoh, N., Kimoto, S., Sugimura, R., Imasu, R., Kawakami, S., Shiomi, K., Kuze, A., Machida, T., Sawa, Y. and
641 Matsueda, H.: Algorithm update of the GOSAT/TANSO-FTS thermal infrared CO₂ product (version 1) and
642 validation of the UTLS CO₂ data using CONTRAIL measurements, *Atmos. Meas. Tech.*, 9(5), 2119-2134,
643 2016.

644 Stephens, B. B., Gurney, K. R., Tans, P. P., Sweeney, C., Peters, W., Bruhwiler, L., Ciais, P., Ramonet, M.,
645 Bousquet, P., Nakazawa, T., Aoki, S., Machida, T., Inoue, G., Vinnichenko, N., Lloyd, J., Jordan, A., Heimann,
646 M., Shibistova, O., Langenfelds, R. L., Steele, L. P., Francey, R. J. and Denning, A. S.: Weak northern and
647 strong tropical land carbon uptake from vertical profiles of atmospheric CO₂, *Science*, 316(5832), 1732-1735,
648 2007.

649 Sweeney, C., Karion, A., Wolter, S., Newberger, T., Guenther, D., Higgs, J. A., Andrews, A. E., Lang, P. M., Neff,
650 D., Dlugokencky, E., Miller, J. B., Montzka, S. A., Miller, B. R., Masarie, K. A., Biraud, S. C., Novelli, P. C.,
651 Crotwell, M., Crotwell, A. M., Thoning, K. and Tans, P. P.: Seasonal climatology of CO₂ across North America
652 from aircraft measurements in the NOAA/ESRL Global Greenhouse Gas Reference Network, *J. Geophys. Res.*
653 *Atmos.*, 120(10), 5155-5190, 2015.

654 Tanaka, M., Nakazawa, T. and Aoki, S.: Concentration of atmospheric carbon-dioxide over Japan, *J. Geophys. Res.*
655 *Ocean.*, 88(C2), 1339-1344, DOI: 10.1029/JC088iC02p01339, 1983.

656 Tanaka, T., Miyamoto, Y., Morino, I., Machida, T., Nagahama, T., Sawa, Y., Matsueda, H., Wunch, D., Kawakami,
657 S. and Uchino, O.: Aircraft measurements of carbon dioxide and methane for the calibration of ground-based
658 high-resolution Fourier Transform Spectrometers and a comparison to GOSAT data measured over Tsukuba
659 and Moshiri, *Atmos. Meas. Tech.*, 5(8), 2003-2012, 2012.

660 Tans, P. P., Conway, T. J. and Nakazawa, T.: Latitudinal distribution of the sources and sinks of atmospheric
661 carbon-dioxide derived from surface observations and an atmospheric transport model, *J. Geophys. Res.*
662 *Atmos.*, 94(D4), 5151-5172, 1989.

663 Tans, P. P., Fung, I. Y. and Takahashi, T.: Observational constraints on the global atmospheric CO₂ budget, *Science*,
664 247(4949), 1431-1438, 1990.

665 Thoning, K. W., Tans, P. P. and Komhyr, W. D.: Atmospheric carbon-dioxide at Mauna Loa observatory. 2.
666 Analysis of the NOAA GMCC data, 1974-1985, *J. Geophys. Res. Atmos.*, 94(D6), 8549-8565, 1989.

667 Washenfelder, R. A., Toon, G. C., Blavier, J. F., Yang, Z., Allen, N. T., Wennberg, P. O., Vay, S. A., Matross, D.
668 M. and Daube, B. C.: Carbon dioxide column abundances at the Wisconsin Tall Tower site, *J. Geophys. Res.*
669 *Atmos.*, 111, D22305, doi:10.1029/2006JD007154, 2006.

670 Wofsy, S. C.: HIPPO Pole-to-Pole Observations (HIPPO): finegrained, global-scale measurements of climatically
671 important atmospheric gases and aerosols, *Philos. T. R. Soc. A*, 369, 2073-2086, doi:10.1098/rsta.2010.0313,
672 2011.

673 Wunch, D., Wennberg, P. O., Toon, G. C., Keppel-Aleks, G., and Yavin Y. G.: Emissions of greenhouse gases from
674 a North American megacity, *Geophys. Res. Lett.*, 36, L15810, doi:10.1029/2009GL039825, 2009.

675 Wunch, D., Toon, G. C., Wennberg, P. O., Wofsy, S. C., Stephens, B. B., Fischer, M. L., Uchino, O., Abshire, J. B.,
676 Bernath, P., Biraud, S. C., Blavier, J. F. L., Boone, C., Bowman, K. P., Browell, E. V., Campos, T., Connor, B.
677 J., Daube, B. C., Deutscher, N. M., Diao, M., Elkins, J. W., Gerbig, C., Gottlieb, E., Griffith, D. W. T., Hurst,
678 D. F., Jimenez, R., Keppel-Aleks, G., Kort, E. A., Macatangay, R., Machida, T., Matsueda, H., Moore, F.,
679 Morino, I., Park, S., Robinson, J., Roehl, C. M., Sawa, Y., Sherlock, V., Sweeney, C., Tanaka, T. and Zondlo,

680 M. A.: Calibration of the Total Carbon Column Observing Network using aircraft profile data', *Atmos. Meas.*
681 *Tech.*, 3(5), 1351-1362, 2010.

682 Wunch, D., Toon, G. C., Blavier, J.-F. L., Washenfelder, R. A., Notholt, J., Connor, B. J., Griffith, D. W. T.,
683 Sherlock, V., and Wennberg, P. O.: The total carbon column observing network, *Philosophical Transactions of*
684 *the Royal Society - Series A: Mathematical, Physical and Engineering Sciences*, 369(1943), 2087-2112,
685 doi:10.1098/rsta.2010.0240, 2011.

686 Wunch, D., Wennberg, P. O., Messerschmidt, J., Parazoo, N. C., Toon, G. C., Deutscher, N. M., Keppel-Aleks, G.,
687 Roehl, C. M., Randerson, J. T., Warneke, T., and Notholt, J.: The covariation of Northern Hemisphere
688 summertime CO₂ with surface temperature in boreal regions, *Atmos. Chem. Phys.*, 13, 9447-9459,
689 doi:10.5194/acp-13-9447-2013, 2013.